

Corrosion Protection of Phenolic-Epoxy/Tetraglycidyl Metaxylediamine Composite Coatings in a Temperature-Controlled Borax Environment

Wenhua Xu, Zhenyu Wang, En-Hou Han, and Chunbo Liu

(Submitted January 25, 2017; in revised form June 20, 2017; published online November 7, 2017)

The failure behavior for two kinds of phenolic-epoxy/tetraglycidyl metaxylediamine composite coatings in 60 °C borax aqueous solution was evaluated using electrochemical methods (EIS) combined with scanning electron microscopy, confocal laser scanning microscope, water immersion test, and Raman spectrum. The main focus was on the effect of curing agent on the corrosion protection of coatings. Results revealed that the coating cured by phenolic modified aromatic amine possessed more compact cross-linked structure, better wet adhesion, lower water absorption ($0.064 \text{ mg h}^{-1} \text{ cm}^{-2}$) and its impedance values was closed to $10^8 \Omega \text{ cm}^2$ after immersion for 576 h, while the coating cured by modified aromatic ring aliphatic amine was lower than $10^5 \Omega \text{ cm}^2$. The corrosion mechanism of the two coatings is discussed.

Keywords alkaline corrosion, corrosion protection, EIS, organic coatings, phenolic modified aromatic amine

1. Introduction

As a vital chemical raw material, borax is widely used in glass, enamel, chemical engineering, medicine and other industries, and plays an indispensable role in the fields of defense and aerospace. However, borax causes serious corrosion not only where they are produced, but used. For example, when LOCA (Loss of coolant accident) happens in nuclear power plant, a large amount of borax aqueous solution will be sprayed on the surface of containment, and containment cannot meet the requirements of corrosion resistance without the excellent protection. Even though metal or inorganic coatings possess better anticorrosion performance, high cost of fabricating and constructing restricts their application. By comparison, the application of organic coatings is a cost-effective way to inhibit the process of corrosion (Ref 1).

In the large family of organic coatings, phenolic-epoxy is suitable for certain uses in corrosive condition. It combines the advantages of both phenolic resins and epoxy resins (Ref 2), and encompasses an array of unique properties such as excellent heat resistance, chemical resistance and good mechanical properties (Ref 3-5). However, poor toughness,

low thermal stability (Ref 6), and inherent brittleness (Ref 5) have greatly limited pervasive application of traditional PR (phenolic resin). To strike a balance between the thermal resistance and toughness of PR, tetraglycidyl metaxylediamine is taken into account. Relevant literature (Ref 7) declares that when tetraglycidyl metaxylediamine polymer is blended with this siloxane- or imide-containing tetrafunctional epoxy, the cured material apparently shows enhanced thermal properties and toughness, but lower residual stress. To the best of our knowledge, there are few reports on phenolic-epoxy resin and tetraglycidyl metaxylediamine polymer used together as the binder of corrosion-inhibiting coating. Therefore, the research on phenolic-epoxy resins and tetraglycidyl metaxylediamine polymer used together in borax aqueous solution is vital to the field of nuclear power and other alkaline industrial environment.

In this work, we chose 60 °C as the working temperature and used 0.1 mol/L borax ($\text{Na}_2\text{B}_4\text{O}_7 \cdot 10\text{H}_2\text{O}$) aqueous solution for tests, according to the practical corrosive environment in conventional island in a nuclear power plant. The performance of phenolic-epoxy/tetraglycidyl metaxylediamine coatings with different amine curing agents used in borax aqueous solution was reported. The electrochemical impedance spectra (EIS), laser Raman spectroscopy, contact angle analysis and surface characterization techniques (SEM) were utilized to characterize the anticorrosive performance of the composite coatings in borax aqueous solution.

2. Experimental

2.1 Sample Preparation

Tetraglycidyl metaxylediamine (EEW: 95-105 g/eq, viscosity (25 °C): 2200-2600 mPa s, proportion (25 °C): 1.15, and COC > 220), bisphenol-F phenolic-epoxy (EEW: 172-179 g/eq, viscosity (51.7 °C): 1100-1700 mPa s, and density (25 °C): 1.21 g/mL), phenolic modified aromatic amine (HN01) (amine value: $290 \pm 10 \text{ KOH mg/g}$, viscosity (25 °C): 960 mPa s, and

Wenhua Xu, Key Laboratory of Nuclear Materials and Safety Assessment, Institute of Metal Research, Chinese Academy of Sciences, 62 Wencui Road, Shenyang 110016, China; and University of Chinese Academy of Sciences, 19 Yuquan Road, Beijing 100049, China; **Zhenyu Wang**, and **En-Hou Han**, Key Laboratory of Nuclear Materials and Safety Assessment, Institute of Metal Research, Chinese Academy of Sciences, 62 Wencui Road, Shenyang 110016, China; and **Chunbo Liu**, China Key Center for Wear and Corrosion Resistant Materials, Huadian Zhengzhou Mechanical Design Institute Co., Ltd, 19 Huaihe East Road, Zhengzhou 450015, China. Contact e-mail: zzyywang@imr.ac.cn.

AHEW: 86), and modified aromatic ring aliphatic amine (FJ02) (amine value: 390 ± 410 KOH mg/g, viscosity (25 °C): 300–380 mPa s, proportion (25 °C): 1, and AHEW: 68).

The composition of coatings is listed in Table 1. Coating 1 used composite resin (m (bisphenol-F phenolic-epoxy resins): m (tetraglycidyl metaxylediamine) = 4:1) as the binder and consisted of layers 1A and 1B. Layer 1A was filled with some additives and fillers, and 1B was applied for the hole sealing varnish. Coating 1 used modified aromatic ring aliphatic amine (FJ02) as curing agent. For coating 2, phenolic modified aromatic amine (HN01) was used as curing agent, and all other components were same as coating 1. Layer B for coatings 1 and 2 was mixed and ground for 7 h in a ball mill, and applied to substrate by spray painting, respectively. The coated plates with layer B were dried at room temperature for 24 h. Subsequently, layer A for coatings 1 and 2 was sprayed on them, respectively. The final samples were dried at room temperature for 24 h and then dried in an air-circulating oven at 50 °C for 8 h to ensure that the coatings cured completely without any resident solvent. Abrasive blasted Q235 steel plates with size of 150 mm × 75 mm × 2 mm were used as substrates for corrosion immersion test, and the dimension of sample plate for EIS experiment was 50 mm × 50 mm. The final thickness of the coated films was in the 400 ± 5 μm for water immersion test and 80 ± 5 μm for EIS test.

2.2 Water Immersion and Wet Adhesion Test

Water immersion (static) test of coatings is a conventional approach to evaluate corrosion resistance of coatings. Before immersion, the edges of all specimens were sealed to prevent any possible influence on test results by samples. The coating-coated carbon steel plates were immersed in 0.1 mol/L borax ($\text{Na}_2\text{B}_4\text{O}_7 \cdot 10\text{H}_2\text{O}$) aqueous solution at 60 °C for 25 days, and photographs were taken every 5 days. Six parallel samples were prepared for a coating, and the samples before taking photographs were dried at 30 °C for 4 h in a furnace.

Meanwhile, the samples after immersion and drying process were used for pull-off test (PosiTest AT-M) to test the wet adhesion every 5 days. The coating surfaces were ground by emery paper (#240) to enhance the mechanical anchoring of the glue (Araldite) which attaches the stud perpendicularly to the coating surface. After application, the glue was cured at room temperature for 2 days and 40 °C for 4 h in an air-circulating oven to ensure that the adhesive was cured completely and would not fail during the test. At least six measurements were taken for each sample, and their average value was taken as the final result.

Table 1 Composition of coatings

Sample	Composition
Coating 1	
1A	65% composite polymer, 7% Sb_2O_3 , 0.8% carbon black, 0.5% KH550 silane coupling agent, 19.3% 240 mesh flake, 7% 800 mesh SiC, 0.4% BYK106 dispersant, 26.75% FJ02 curing agent
1B	100% composite polymer, 41.15% FJ02 curing agent
Coating 2	
2A	65% composite polymer, 7% Sb_2O_3 , 0.8% carbon black, 0.5% KH550 silane coupling agent, 19.3% 240 mesh flake, 7% 800 mesh SiC, 0.4% BYK106 dispersant, 34% HN01 curing agent
2B	100% composite polymer, 52% HN01 curing agent

2.3 Gravimetric Experiment

In order to create free films, the liquid concoction of layer B for coatings 1 and 2 was transferred to the same plastic mold, respectively. They were dried at room temperature for 24 h and then dried in air-circulating oven at 50 °C for 8 h. After wiping off molds, free films were successively abraded with 240, 400, and 1000 grit emery papers to remove the parts of coatings cured incompletely and then cleaned thoroughly with deionized water, respectively. Finally free films were dried in air-circulating oven at 30 °C for 24 h to prepare for the next test. The diameter of free film for each coating was 50.00 ± 0.50 mm, and the thickness was 8.00 ± 0.50 mm.

Free films were immersed into 0.1 mol/L borax ($\text{Na}_2\text{B}_4\text{O}_7 \cdot 10\text{H}_2\text{O}$) aqueous solution at 60 °C. During the test, the specimens were pulled out of the water bath and weighted periodically at room temperature using an analytical balance with a precision of 0.0001 g. Excessive surface water was removed by blot-drying the samples using a filter paper just prior to any weight measurement. The test solution was regularly renewed, and a plastic wrap was placed onto the glass vessel to avoid evaporation. To guarantee the authenticity and repeatability of the test data, three samples were used for each test. The water absorption (%) was then calculated using the equation:

$$Q_t = \frac{m_t - m_0}{m_0} \times 100\% \quad (\text{Eq 1})$$

where m_t is the mass of free film at time t , and m_0 is the mass before immersion.

2.4 Surface Properties

Water contact angle (WCA) on the coatings was measured using a JC2000D2 contact angle goniometer at room temperature, and deionized water was used as the test liquid. To obtain reliable contact angle data, three droplets were dispensed at different surface parts of the sample and the reported value was the average.

The surface and cross-section samples were cut out of the coated plates before and after static immersion test. In the case of cross section, it was embedded in bakelite by using XQ-2B mounting press in order to grind with SiC paper up to 2000 grade and then polish. The surface and cross section of the selected specimens were analyzed by scanning electron microscopy (SEM, XL30-FEG-ESEM) at 20 kV equipped with energy-dispersive spectrometer (EDS) to evaluate element distribution of corrosion products layer, and a gold film was sprayed atop the surface of specimen to make it electrically conductive.

The three-dimensional morphology and the surface roughness of coatings were examined by confocal laser scanning microscope (OLYMPUS 4000). Mean roughness (R_a) was calculated from three different positions for each sample.

2.5 Electrochemical Studies

Electrochemical properties of the coatings were investigated in 60 °C using an electrochemical workstation (PAR273A, USA). Measurements were taken in a three-electrode cell with 0.1 mol/L borax aqueous solution as an electrolyte. The three-electrode cell included a saturated calomel reference electrode (SCE) filled with saturated KCl solution which served as a reference electrode (RE), a platinum auxiliary electrode with an exposure surface of 13 mm × 13 mm as a counter electrode (CE), and the sample with an exposure surface of 12.56 cm² as working electrode (WC). Prior to the electrochemical measurements, the samples were kept in the solution for 30 min in order to stabilize the free corrosion potential.

The electrochemical impedance spectroscopy (EIS) measurements were taken at open circuit potential in an applied frequency ranged from 100 kHz to 10 mHz, and the sinusoidal perturbation signal with 20-mV amplitude was used. The obtained data were interpreted on the basis of equivalent electrical analogs using Zsimpwin to obtain the fitting parameters.

2.6 Raman Spectrum

Raman spectrum was obtained in a total reflection pattern in a wavenumber range of 4000-250 cm⁻¹, using an excitation wavelength of 532 nm, a laser power of 0.03 mW, and a signal accumulation time of 0.5 s.

3. Results and Discussion

3.1 Curing Mechanisms of Coatings

The reaction mechanisms for phenolic-epoxy and GA-240 with different curing agents are presented in Schemes 1 and 2, which involves epoxy group reacting with reducing hydrogen in amidogen to generate -C-N-. Since HN01 possesses more reducing hydrogen in one molecule than FJ02, the system cured

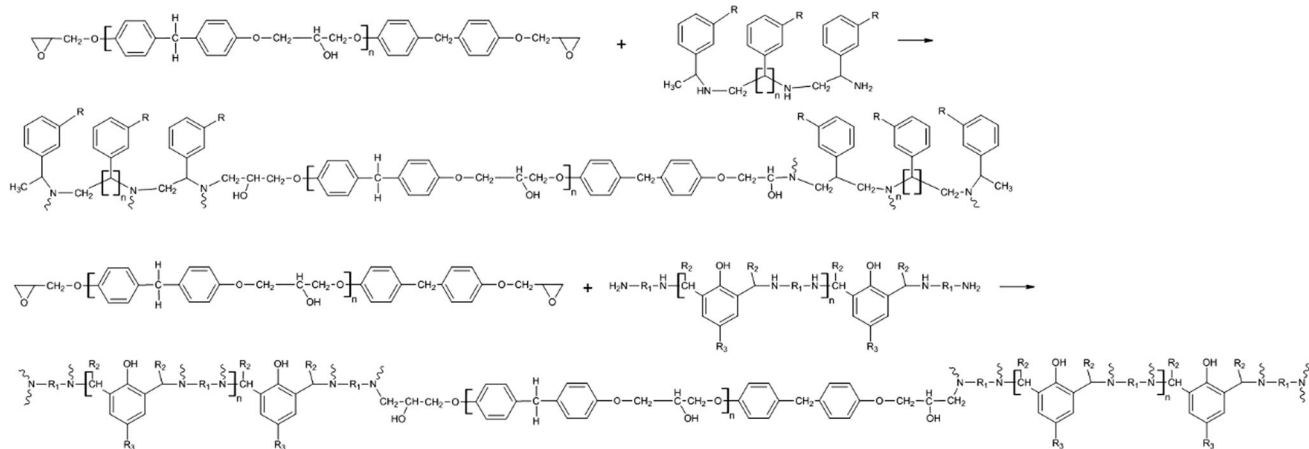
by HN01 reacts more thoroughly under room temperature. Furthermore, the molecular chain for HN01 is much longer than for FJ02. As a result, the cured products for coating 2 generate a more complicated three-dimensional conformation easily to obtain more compact cross-linked structure, which provides relevant support in further work for better corrosion resistance of coating 2.

3.2 Surface Wettability

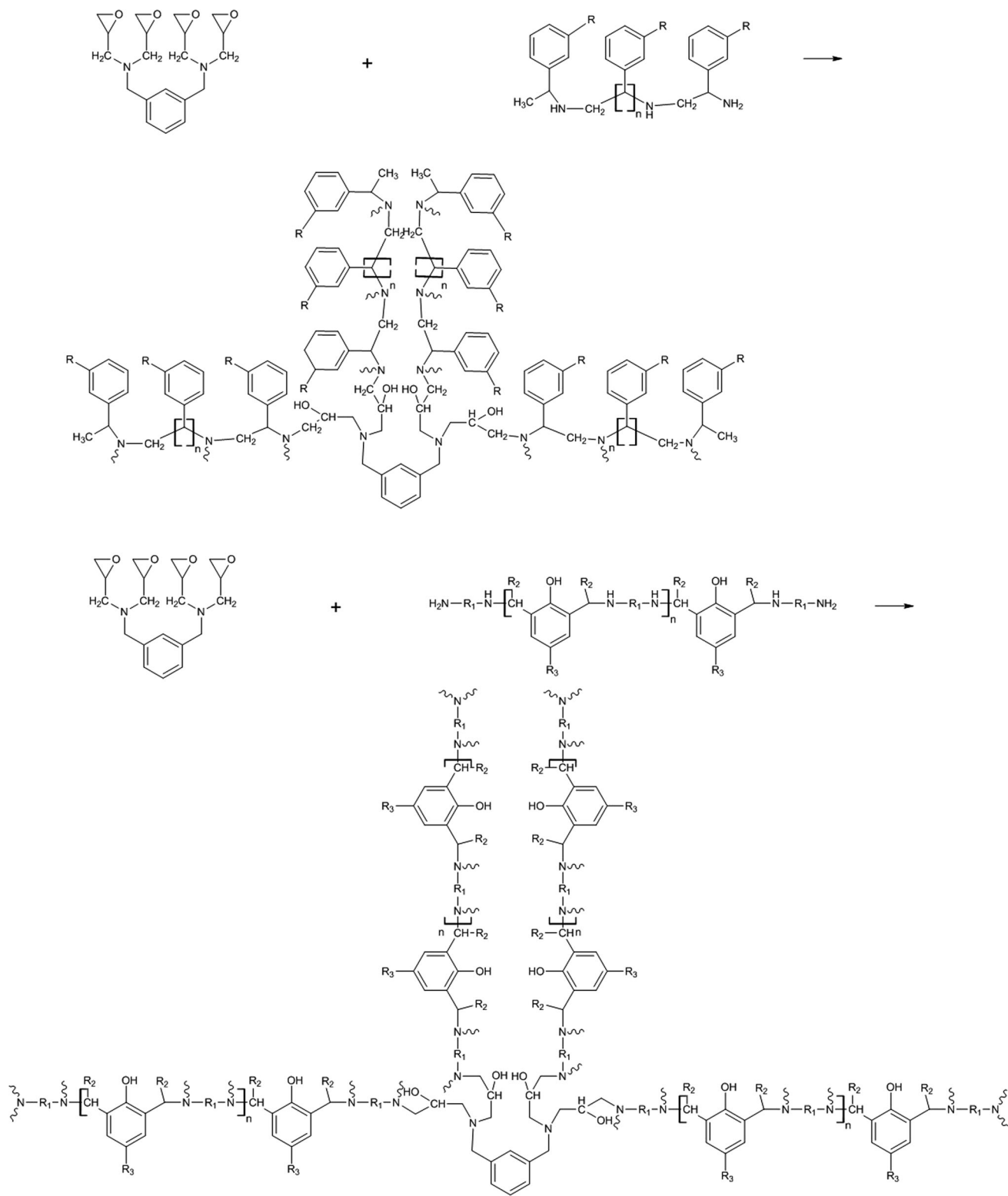
Figure 1 shows the evolution of contact angles for the surface of coating 1 and 2 with immersion time. The same hydrophilic characteristic is displayed for the two coatings, in every case, with contact angle values lower than 90° (Ref 8), which is associated with the density of hydroxyl groups on the surface of the coating. The results show that contact angles for coating 1 and coating 2 appear increasing at first and then decreasing as time prolonged. The peak value is 78.8° for coating 1 obtained on the 20th day, and 82.0° for coating 2 acquired on the 15th day. After reaching the peak value, the contact angle of coating 1 decays rapidly, while coating 2 turns to a slow decay. All these reveal that the coating structure cured by HN01 curing agent brings better surface effect than that cured by FJ02 curing agent, which offers another perspective on the less water sorption for coating 2 than for coating 1.

3.3 Water Absorption

Since water absorption in organic coatings can lead to loss of adhesion, formation of osmotic blisters, and establishment of a pathway for corrosive ions (Ref 9), it is considered to be the primary cause for initiation of corrosion and can be studied in detail by gravimetric tests. Figure 2(a) shows the characteristics of water absorption ($M_t/m_0 \times 100\%$) curves for layer B in coatings 1 and 2. M_t is water mass uptake at time t , and m_0 is mass of free film before immersion. It is obvious that water absorption increases at initial stage and then reaches saturation limit for two coatings. During the first stage, layer 1B absorbs water much faster than layer 2B, resulting in more water absorption at the same immersion time. It is noticeable that the saturated water absorption obtained for layer 1B is 2.99%, while that of layer 2B is only 1.66%, implying that layer 2B decreases effectively the water absorption.



Scheme 1 Curing mechanism of phenolic-epoxy polymers and two curing agents (aromatic ring aliphatic amine and phenolic modified aromatic amine)



Scheme 2 Curing mechanism of tetraglycidyl metaxyliediamine polymer and two curing agents (aromatic ring aliphatic amine and phenolic modified aromatic amine)

To identify the diffusion type for layers B cured by different curing agents, gravimetric results are presented by plots of water mass uptake (M_t) or relative water mass uptake (M_t/M_∞) as a function of square root of time ($t^{1/2}$), and water absorption

curves are also fitted by $y = Ax^B$ model. M_t and M_∞ are water mass uptake at time t and after saturation. Previous research (Ref 10) shows that Fick sorption includes three characteristic features: (1) an initially linear plot of M as a function of $t^{1/2}$, (2)

with increasing t , the water mass curve smoothly levels off to a saturation level M_∞ , (3) when M_t/M_∞ is plotted as a function of $t^{1/2}/l$ (where l is the film thickness), a “reduced” plot is

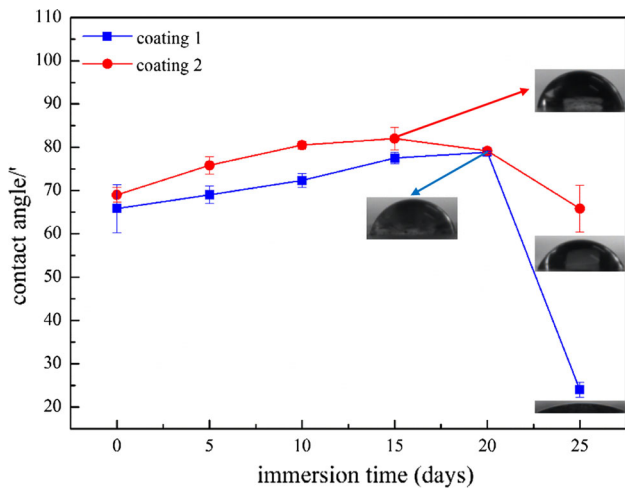


Fig. 1 Contact angle measurement for water of coatings 1 and 2 with immersion time

obtained, which is identical for different values of film thickness. The variations of M_t and M_t/M_∞ satisfy the three features well, as shown in Fig. 2(b) and (c), and should be classified as Fick diffusion. According to variations of M_t/M_∞ , there are no obvious characteristics of two stages absorption, S shape absorption and II diffusion appearance (Ref 10, 11). In addition, the fitting results show that the index B for layer 1B (0.50999) is close to 0.5, implying that the diffusion type is an ideal Fick diffusion, whereas B for layer 2B (0.39987) deviated from 0.5 to some degree, indicating that the diffusion type is the non-ideal Fick diffusion (Ref 12). Therefore, curing agent HN01 changes the diffusion type of water absorption of coatings from an ideal diffusion to a non-ideal diffusion.

The average diffusion velocity $V_a(M_t/St)$ for the whole immersion time is also calculated after the division process of water absorption curve, as shown in Fig. 2(d). M_t is water mass uptake at time t , S is the area of coatings, and t is the immersion time. At the beginning, V_a for layers 1B and 2B are relatively fast because water absorption occurs at the free surface of the material. Later this process slows down because of the saturation of surface water, and the exterior water tends to diffuse into the interior (Ref 13). During the subsequent immersion period, V_a decreases gradually with immersion time

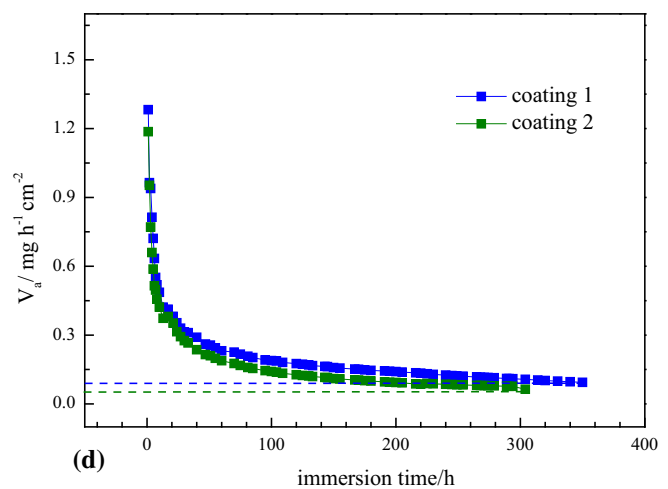
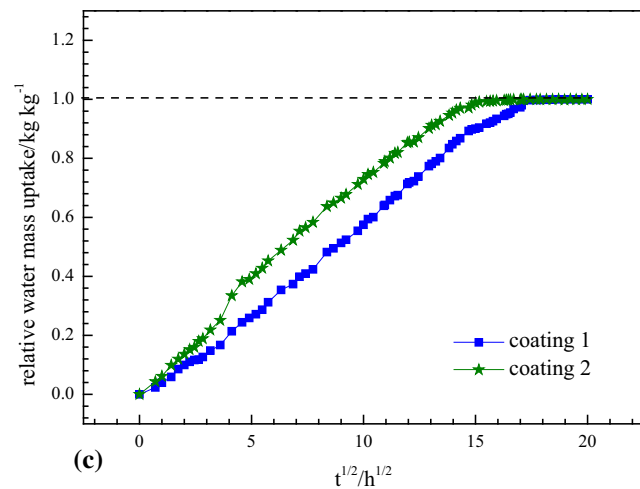
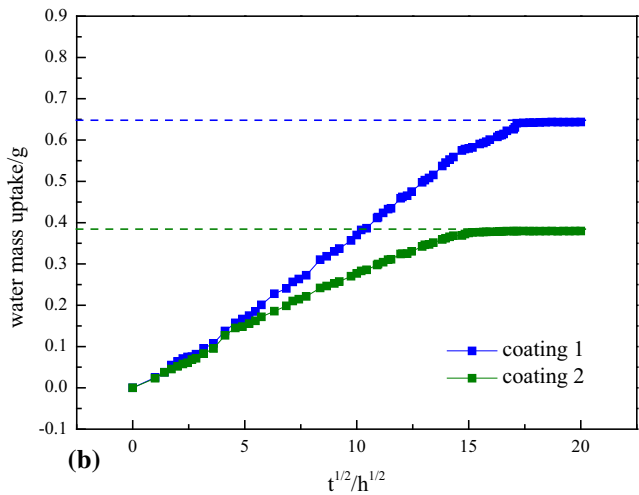
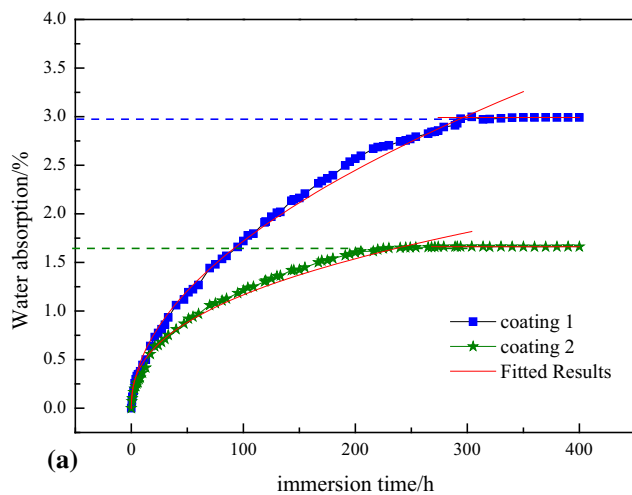


Fig. 2 Water absorption $\sim t$ curves and fitting results (a), water mass uptake $M_t \sim t^{1/2}$ curves (b), relative water mass uptake $M_t/M_\infty \sim t^{1/2}$ curves (c), and average water diffusion velocity, V_a (d) for layer B in coatings 1 and 2

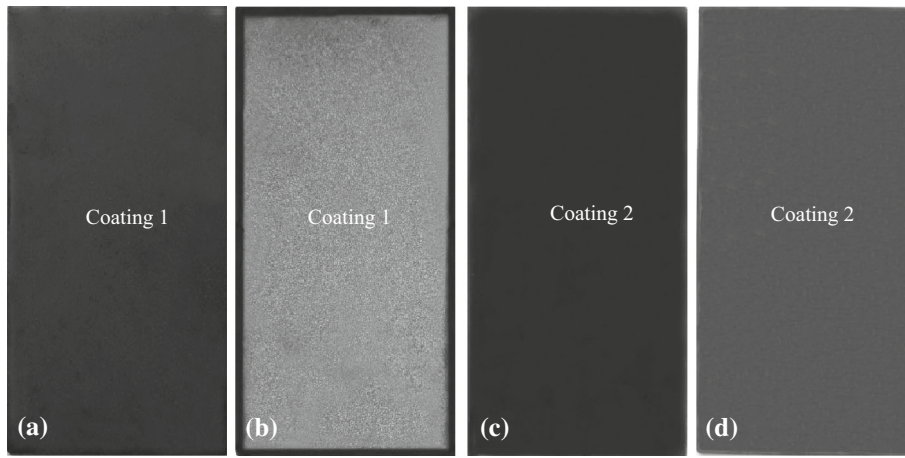


Fig. 3 Photographs of coatings 1 and 2 before (a, c) and after (b, d) immersion for 25 days

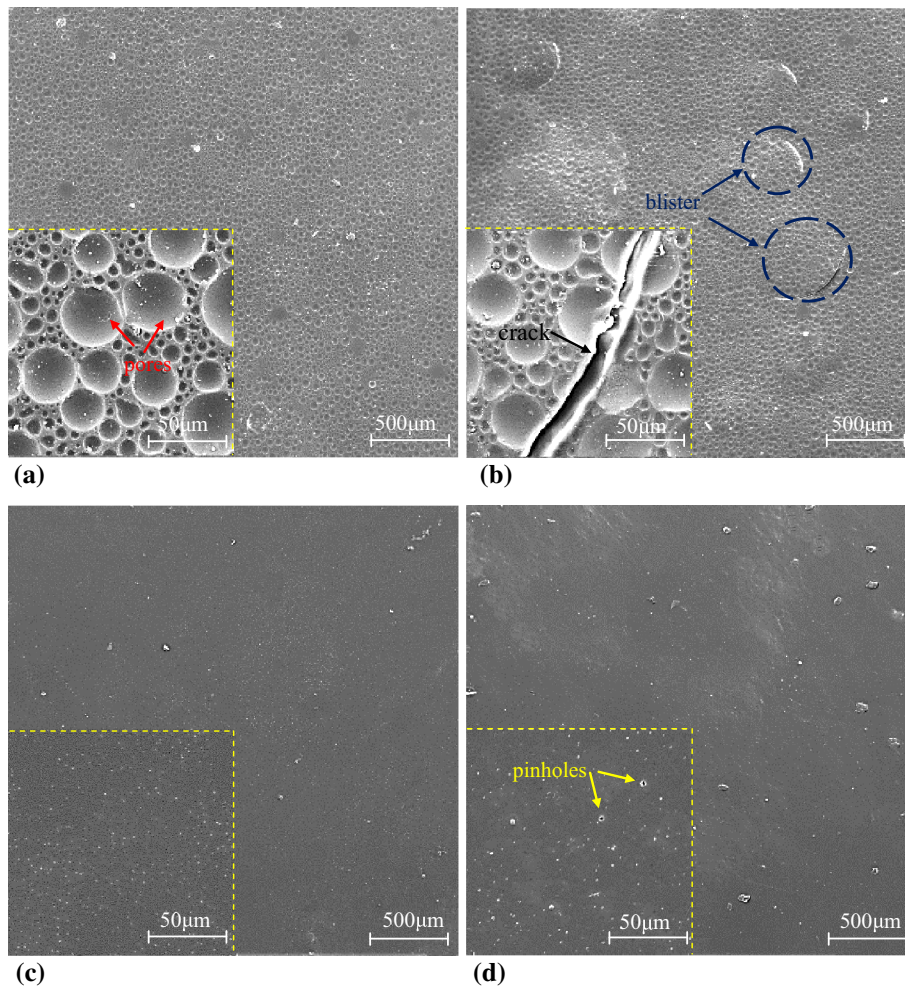


Fig. 4 SEM images of the surface morphologies for coatings: coating 1 before (a) and after (b) immersion for 25 days, and coating 2 before (c) and after (d) immersion for 25 days

(from 1.28 to 0.094 $\text{mg h}^{-1} \text{cm}^{-2}$ for layer 1 and from 1.19 to 0.064 $\text{mg h}^{-1} \text{cm}^{-2}$ for layer 2), and V_a for layer 2B is obviously slower than layer 1B. Therefore, high water diffusion velocity is responsible for rapid water absorption through coatings (Ref 12), and layer 2B can slow down effectively the water absorption and transport.

3.4 Surface Morphology Observation

Figure 3 shows the photographs of coating 1 and 2 before and after immersed for 25 days. Blistering is the main phenomena of coating 1 after immersion (Fig. 3b), which causes a severe coating damage. The most noteworthy reason

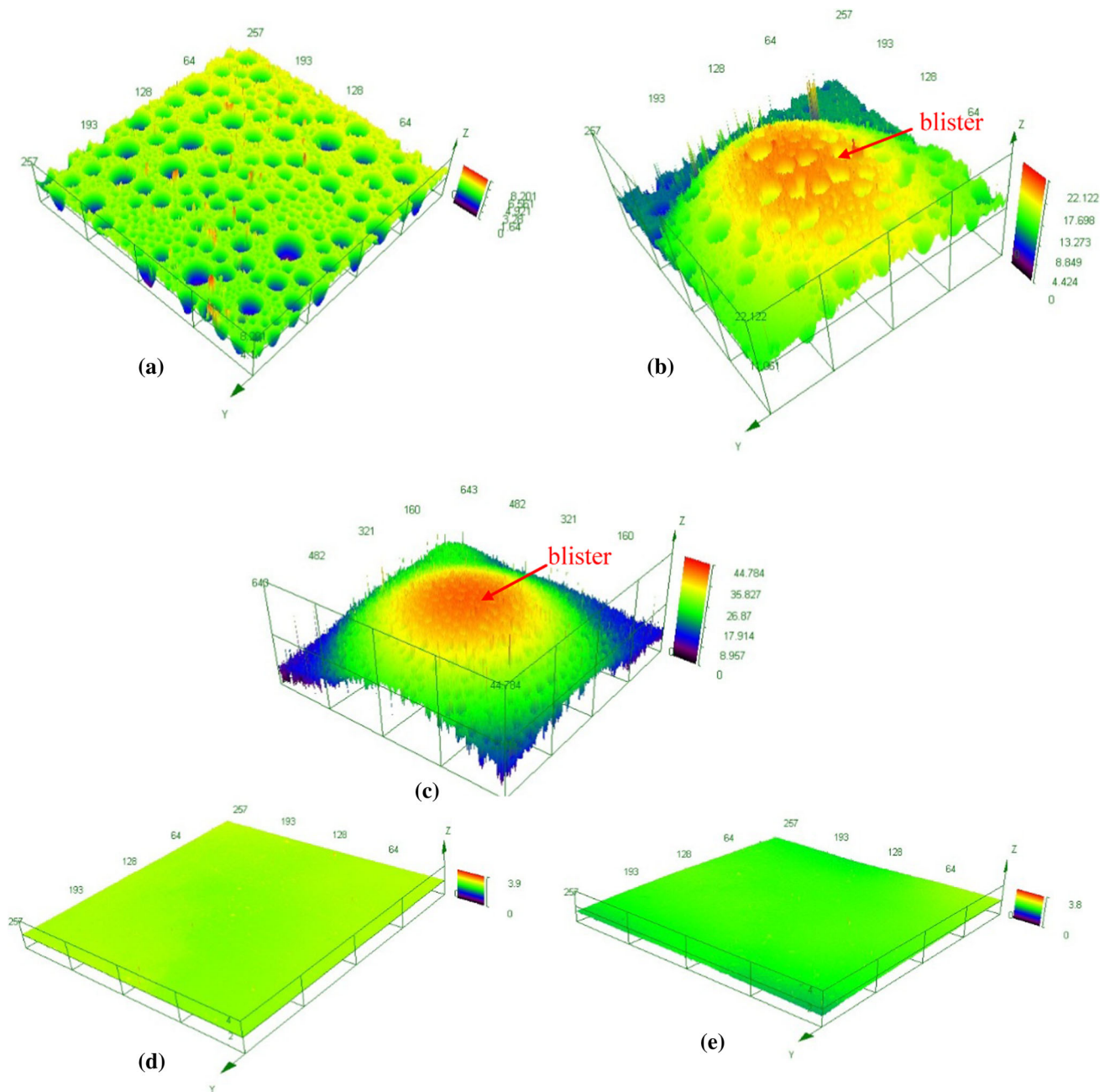


Fig. 5 3D confocal images of coatings: coating 1 before (a) and after (b) immersion for 25 days at high magnification, the low-magnification image (c) corresponding to (b) as supplementary, and coating 2 before (d) and after (e) immersion for 25 days at high magnification

for blistering is that the corrosion reaction between substrate and corrosive medium continues to produce gas, and the gas cannot go through the coating successfully because of the high density of the coating. Discovered through comparative analysis, only slight variations in color can be detected from Fig. 3(c) and (d), which implies the corrosion resistance of coating 2 is superior to coating 1.

SEM images of the surface morphologies for coating 1 and 2 before and after immersion for 25 days are shown in Fig. 4. As seen in Fig. 4(a), non-uniform and interconnected network pore structure appears on the surface of coating 1, and the mechanism for pore phase formation is due to vapor-induced

phase separation (Ref 14). After immersion for 25 days, many cracks emerge (Fig. 4b) because of the tensile stress induced from blistering, and the signs of the presence of blisters can be captured easily. As a comparison, coating 2 produces a dense phase with transparent morphology free of defects (Fig. 4c). After immersion for 25 days, the surface morphologies remain almost unchanged, and only several pinholes can be detected (Fig. 4d). We can conclude that suitable curing agent can provide dense network structure, and make coatings reduce surface defects and improve the corrosion resistance.

For a better representation of the coating topography change, 3D confocal images of coating 1 and 2 before and

after immersed for 25 days are shown in Fig. 5. It is apparent that the surface of coating 1 in the initial state is pitted with subsidence holes, which results in higher surface roughness ($0.634\ \mu\text{m}$) than that of coating 2 ($0.028\ \mu\text{m}$). The smaller the surface roughness of the coatings, the smaller the surface area for the corrosion attack becomes (Ref 15). After immersion for

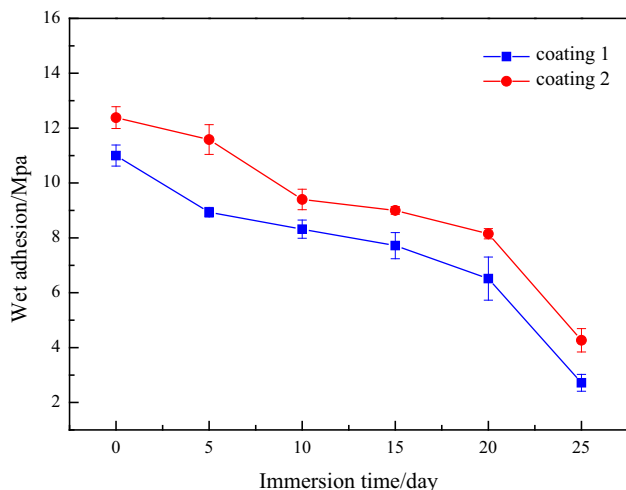


Fig. 6 Changes of wet adhesion for coatings 1 and 2 with immersion time

25 days, an obvious upward bulge can be detected for coating 1 (shown in Fig. 5b), which leads to the increase in surface roughness ($2.394\ \mu\text{m}$), whereas the surface roughness of coating 2 remains constant ($0.026\ \mu\text{m}$). Furthermore, supplementary Fig. 5(c) better shows the surface topography of a complete blister, corresponding to the surface morphology of coating 1 (Fig. 3b and 4b). Thus, we can conclude that coating 2 cured by phenolic modified aromatic amine has a smaller surface roughness, which declines effectively the attack of the corrosive medium.

3.5 Wet Adhesion

As an important mechanical property, once adhesion fails, all other protective mechanisms will become worthless, so the effect of different curing agents on the adhesion strength of coatings should be studied. Figure 6 demonstrates the changes of wet adhesion of coating 1 and 2 with immersion time. The dry adhesion value for coating 1 and 2 is 11.0 and 12.3 MPa, respectively, implying outstanding coating performance. However, it needs to be mentioned that adhesion tests in the dry state are of little use for applications in immersed or humid environments (Ref 14), because the presence of water normally decreases adhesion between the coating and the substrate (Ref 16). During the immersion process, the wet adhesion for both coatings 1 and 2 present a decline in a different degree. After immersion for 25 days, the correspondent wet adhesion has

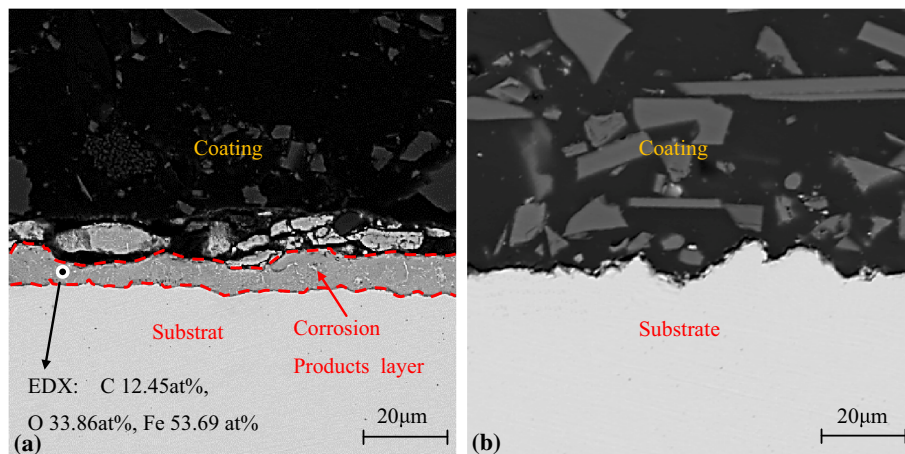


Fig. 7 Cross-section morphologies of interface between metal substrate and coatings 1 (a) and 2 (b) after continuous immersion for 25 days in the borax aqueous solution

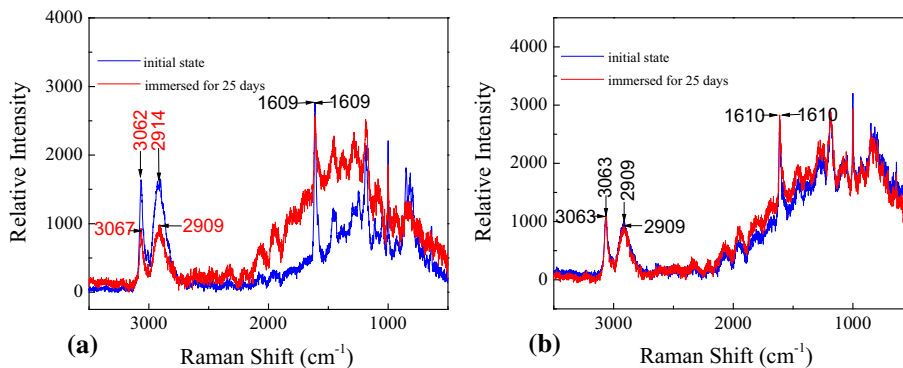


Fig. 8 Raman spectra of coatings 1 (a) and 2 (b) in the initial state and after 0.1 mol/L borax aqueous solution immersion for 25 days

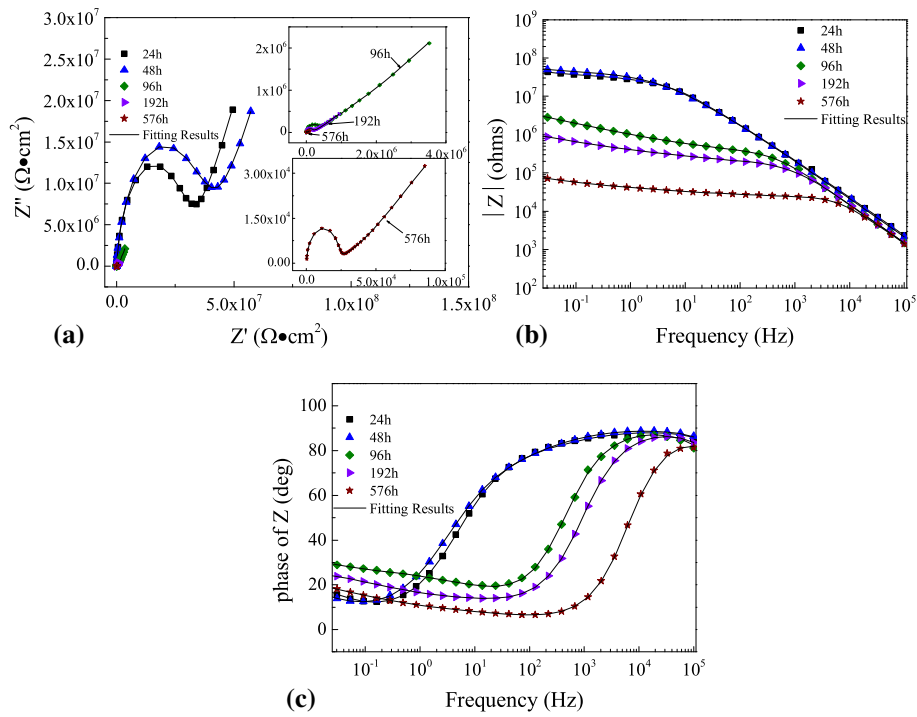


Fig. 9 EIS of coating 1 immersed in 0.1 mol/L borax aqueous solution at 60 °C: Nyquist plots (a), impedance modulus Bode plots (b), and phase angle Bode plots (c)

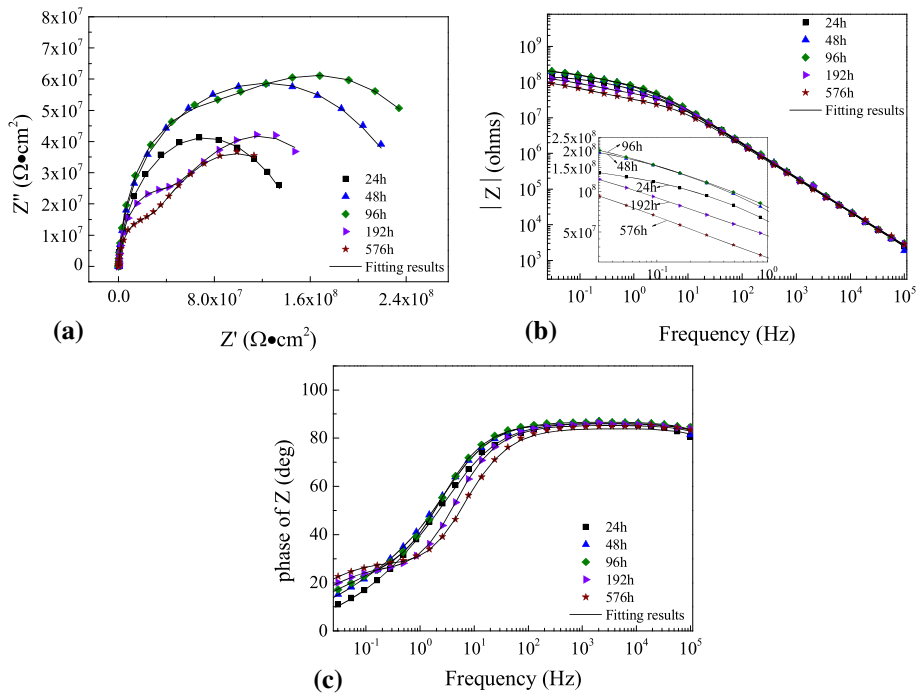


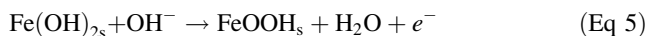
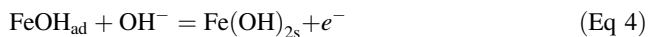
Fig. 10 EIS of coating 2 immersed in 0.1 mol/L borax aqueous solution at 60 °C. Nyquist plots (a), impedance modulus Bode plots (b), and phase angle Bode plots (c)

declined to a very low level. In spite of this, the wet adhesion values for coating 2 (4.3 MPa) is always much higher than that of coating 1 (2.7 MPa), which might be attributed to the fact that coating 2 cured by phenolic modified aromatic amine can reduce the destruction of water to wet adhesion by preventing water absorption through its physical barrier effect.

3.6 Cross Section Morphology Observation

SEM images of the cross section clearly illustrate the interface state of coatings 1 and 2 after immersion for 25 days. As seen in Fig. 7(a), obvious variations in color can be distinguished on the substrate. Subsequently, the EDS analysis of this area with color change shows the presence of elements

like carbon (4.05%), iron (81.26%) and oxygen (14.68%), which reveals the formation of corrosion products layer, and provides the direct evidence for the rapid degradation of adhesion strength. The typical products formed, such as $\text{Fe}(\text{OH})_2$, $\text{Fe}(\text{OH})_3$ or FeOOH , and so on, are dependent on the local pH (accumulation of OH^-) and located in the upper part of the substrate, according to the following sequence (Ref 17).



With respect to the presence of $\text{Fe}(\text{OH})_3$, it is assignable to the oxidation of $\text{Fe}(\text{OH})_2$. This supports that coating 1 has been damaged to some extent during the immersion process.

Compared with coating 1, the structure of coating 2 is more compact, and no corrosion products are detected (visualized in Fig. 7b). In this case, coating 2 remains morphologically unaltered after 25 days of continuous immersion in the electrolyte, which shows good interfacial adhesion and remarkable anticorrosion property.

3.7 Structure Characteristic of Coatings by Raman Spectrum

Raman spectrums of coatings 1 and 2 can be seen in Fig. 8, where the Raman spectrum of coatings for the initial state is compared to that for immersion for 25 days. The peaks at 1610_{-3}^{+2} (marked with arrows in the figure) are assigned as the aromatic ring (Ref 18, 19). Symmetric stretching of NH_4^+ occurred at $2909^{+5} \text{ cm}^{-1}$ and the corresponding asymmetric stretching seen at $3063_{-1}^{+4} \text{ cm}^{-1}$ indicate the existence of NH_4^+ (Ref 20).

After immersion for 25 days, obvious spectral changes can be detected for coating 1 (Fig. 8a), and intensity of several strong bands declines significantly. Clearly, the intensity of symmetric stretching of NH_4^+ at 2909 cm^{-1} and asymmetric stretching of NH_4^+ at 3063 cm^{-1} decreases, but not so much as for the aromatic ring band. These changes are mainly attributed to the dissolution of some components containing benzene ring and NH_3^+ during the process of immersion. Conversely, the Raman spectrum of coating 2 after 25 days of immersion is very similar in the whole region to the spectrum of coatings in the initial state (see Fig. 8b). No obvious decay in the Raman signal is observed, which indicates that the cross-linked structure of coating 2 is very stable.

3.8 EIS Analysis

EIS diagrams measured for coating 1 after 24-, 48-, 96-, 192-, and 576-h tests are presented in Fig. 9. It is observed that all of the Nyquist plots (Fig. 9a) show a depressed semicircle at high-frequency region, followed by a diffusion tail at low-frequency region [Warburg impedance (W)]. The presence of Warburg impedance indicates that the electrochemical reactions become diffusion-controlled (Ref 21). Additionally, the diameters of the semicircles at high-frequency region increase firstly and then decrease with immersion time, while the diffusion tails

Table 2 Fitting results of EIS of coatings 1 and 2 immersed in 0.1 mol/L borax aqueous solution for different immersion times (all the chsq (Chi-square) values are in the range of 1.31×10^{-4} – 4.55×10^{-3})

Sample	Immersion time, h	$R_{\text{sol}}, \Omega \text{ cm}^2$	$Q_{\text{coat}}, \text{S s}^n \text{ cm}^{-2}$	α_{coat}	$\text{Ceff}_{\text{coat}}, \text{F cm}^{-2}$	$R_{\text{por}}, \Omega \text{ cm}^2$	$Q_{\text{di}}, \text{S s}^n \text{ cm}^{-2}$	α_{di}	$R_{\text{di}}, \Omega \text{ cm}^2$	$\text{Ceff}_{\text{di}}, \text{F cm}^{-2}$	$W, \Omega^{-1} \text{ cm}^{-2} \text{ s}^{-0.5}$	Chsq, 10^{-4}
Coating 1	24	122.3	7.84×10^{-10}	0.9889	6.54×10^{-10}	1.44×10^6	2.54×10^{-9}	0.633	3.07×10^7	9.56×10^{-11}	1.51×10^{-7}	14.3
	48	122.2	7.96×10^{-10}	0.9944	7.27×10^{-10}	2.09×10^6	3.53×10^{-9}	0.6076	3.95×10^7	1.43×10^{-10}	1.59×10^{-7}	1.31
	96	185.1	1.09×10^{-9}	0.9979	1.06×10^{-9}	3.04×10^5	5.65×10^{-7}	0.4042	5.67×10^6	1.01×10^{-10}	4.78×10^{-7}	3.97
	192	149.6	1.07×10^{-9}	1	1.07×10^{-9}	1.26×10^5	1.64×10^{-6}	0.2902	1.06×10^6	2.63×10^{-8}	8.74×10^{-7}	4.18
	576	109.9	1.11×10^{-9}	1	1.11×10^{-9}	2.13×10^4	2.35×10^{-5}	0.2755	9.27×10^4	2.21×10^{-6}	1.53×10^{-5}	3.50
Coating 2	24	122.3	1.12×10^{-9}	0.9583	5.63×10^{-10}	3.38×10^7	6.17×10^{-9}	0.5112	1.33×10^8	1.11×10^{-9}	1.11×10^{-9}	12.0
	48	132.9	1.05×10^{-9}	0.9645	5.87×10^{-10}	4.96×10^7	6.40×10^{-9}	0.4985	2.23×10^8	1.65×10^{-9}	1.65×10^{-9}	45.5
	96	116.9	1.07×10^{-9}	0.9569	5.23×10^{-10}	7.15×10^7	9.21×10^{-9}	0.5243	2.41×10^8	4.98×10^{-9}	4.98×10^{-9}	25.3
	192	113.2	1.21×10^{-9}	0.9493	5.20×10^{-10}	4.00×10^7	1.70×10^{-8}	0.5564	1.68×10^8	1.05×10^{-8}	1.05×10^{-8}	22.7
	576	109.1	1.44×10^{-9}	0.935	4.85×10^{-10}	2.37×10^7	2.14×10^{-8}	0.5343	1.56×10^8	1.05×10^{-8}	1.05×10^{-8}	20.1

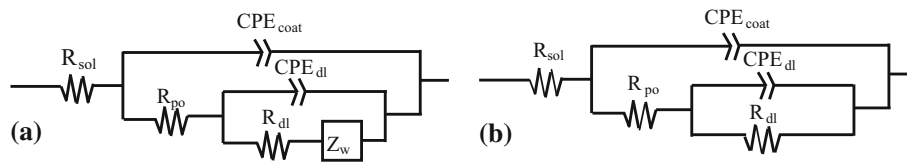


Fig. 11 Equivalent circuit models for coatings 1 (a) and 2 (b)

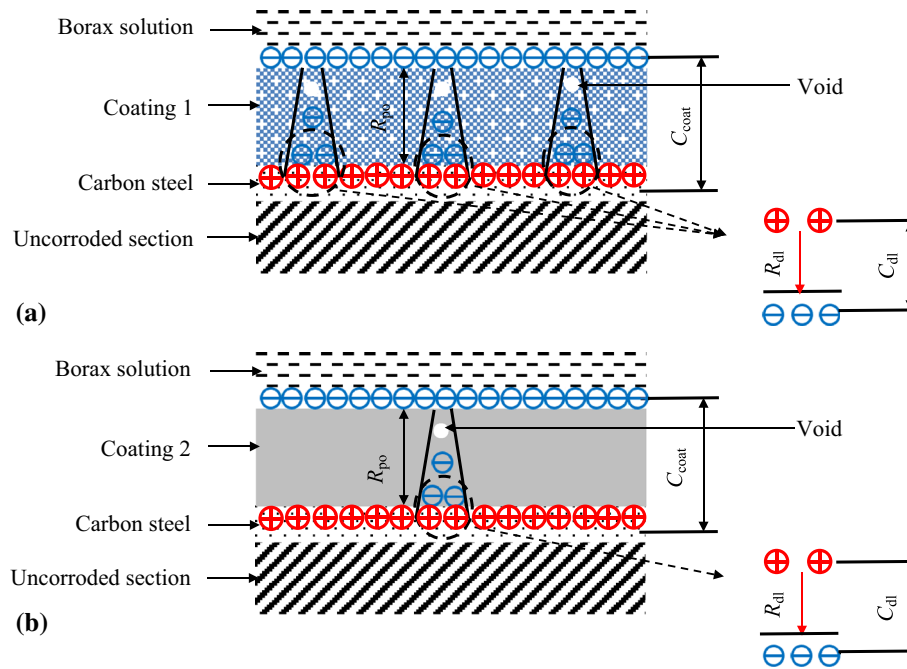


Fig. 12 The corresponding corrosion mechanisms of coatings 1 (a) and 2 (b)

at low frequency enlarge. The variations of the typical impedance modulus Bode diagrams with immersion time are shown in Fig. 9(b). The low-frequency impedance modulus, $|Z|_{LF}$ (e.g., $|Z|_{0.01\text{Hz}}$), is commonly used to roughly estimate the coating resistance (Ref 22). The $|Z|_{0.01\text{Hz}}$ tends to increase in the first 48 h and then decreases steadily, exhibiting the corrosion resistance is strengthened and then weakened. After immersion for 576 h, the modulus at 0.01 Hz decreases below $10^5 \Omega \text{cm}^2$, and a horizontal line section appears at middle frequency, which is the characteristic of delamination of coating (Ref 23, 24). This is ascribed to the bad barrier properties of surface which cannot suppress the penetration of electrolyte solution. Besides, there exist two time constants at different immersion times by observing Fig. 9(c), one at high frequencies that can be associated with the coating and the other at low frequencies related to the underneath corrosive process (Ref 25-28). The time constant at high frequency moves to lower frequency firstly and then to higher frequency, demonstrating the area of coated substrate exposed to the corrosive environment declines firstly and then increases (Ref 29), in accordance with the variation of $|Z|_{0.01\text{Hz}}$ and the Nyquist plots.

The typical EIS spectra of coating 2 with different immersion times are shown in Fig. 10. Being distinct from that of coating 1, only semicircles are presented in the Nyquist spectra of coating 2, which shows that the electrochemical process is under charge transfer control (Ref 30). It is interesting to note that the impedances at low frequency of

the two coatings appear increasing at first and then decreasing gradually, however, with different peak and at different time, which keeps consistent in the variation of the Bode diagrams. The peak which refers to the impedance at which the low frequency reaches a maximum value for coating 1 appearing at 48 h, whereas higher peak value for coating 2 appears at 96 h. Furthermore, even after immersion for 576 h, the $|Z|_{0.01\text{Hz}}$ is still higher than $10^8 \Omega \text{cm}^2$, suggesting remarkably enhanced impedance compared to that of coating 1.

According to ASTM B117 standard test protocol, the service life of a coating is the time taken by the coating to show a drop in the impedance value to $10^6 \Omega \text{cm}^2$. Usually, the service life of the coating can be expressed as 750 h of ASTM B117 with $Z_{0.1\text{Hz}} > 10^6 \Omega \text{cm}^2 = 1$ year of service life. Therefore, the expected service life for coating 2 is at least 280 days, however, only 93 days for coating 1, which demonstrates that phenolic modified aromatic amine can significantly increase the expected service life of coatings.

To quantify the relevant parameters for the corrosion performance, EIS data are fitted by means of equivalent circuits using Z plot for Windows (Ref 31). Since a certain frequency dispersion, as distinct to a pure capacitance, appears in the low-frequency tail of the diffusive response (Ref 32), the electric double layer is gradually deviating from the pure capacitance, and model employed substitutes constant phase elements (CPE) for capacitances. The impedance function of a CPE complies with the following equation (Ref 33-35):

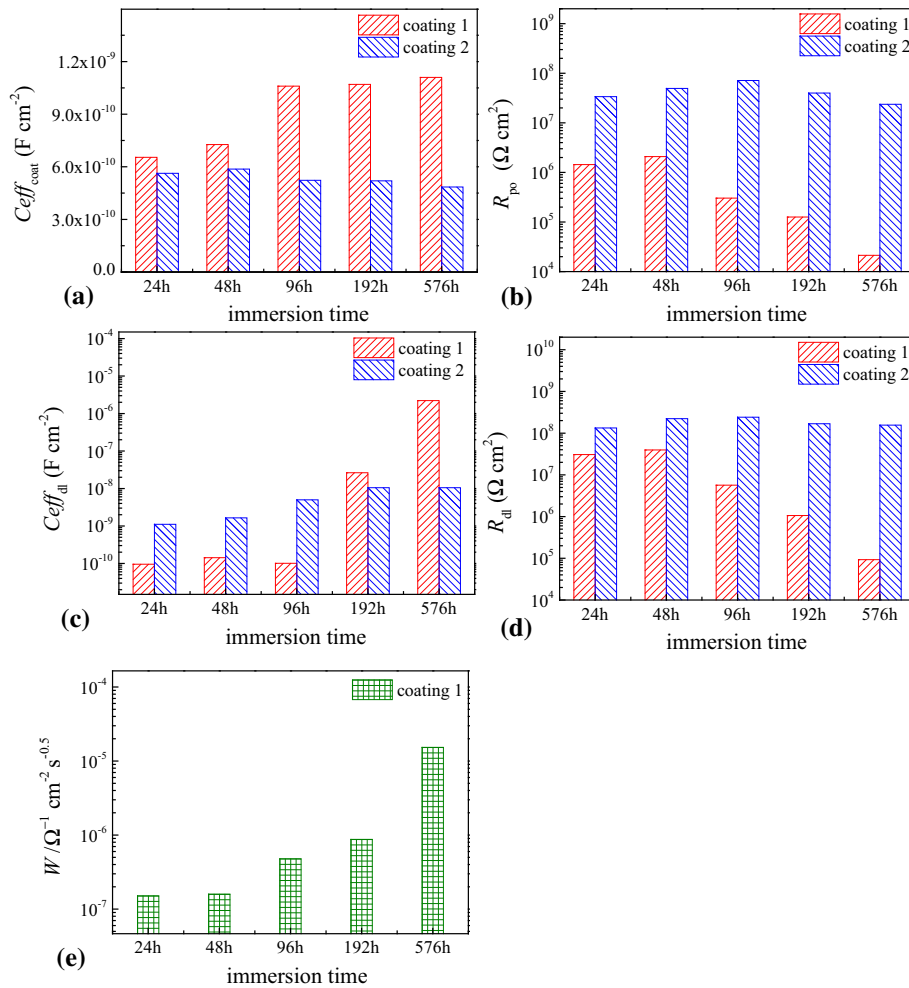


Fig. 13 Variation of $C_{\text{eff,coat}}$ (a), R_{po} (b), R_{dl} (c), $C_{\text{eff,dl}}$ (d), and W (e) for coatings 1 and 2 with immersion time (values from Table 2)

$$Z_{\text{CPE}} = \frac{1}{Q(j\omega)^\alpha} \quad (\text{Eq 6})$$

where Q and α are the CPE constant, ω is the angular frequency (in rad/s), $j = (-1)^{1/2}$, and α is a CPE exponent associated with surface heterogeneity or roughness (Ref 36). When $\alpha < 1$, the CPE parameter cannot represent the capacitance, and the effective capacitance (C_{eff}) of the coating associated with the CPE can therefore be expressed as (Ref 37):

$$C_{\text{eff,coat}} = Q_{\text{coat}}^{\frac{1}{\alpha_{\text{coat}}}} \left(\frac{R_{\text{sol}} \cdot R_{\text{po}}}{R_{\text{sol}} + R_{\text{po}}} \right)^{\frac{1-\alpha_{\text{coat}}}{\alpha_{\text{coat}}}} \quad (\text{Eq 7})$$

Similarly, $C_{\text{eff,dl}}$ describes the effective capacitance of the inner layer between the bottom of pores and the metal substrate:

$$C_{\text{eff,dl}} = Q_{\text{dl}}^{\frac{1}{\alpha_{\text{dl}}}} \left(\frac{R_{\text{po}} \cdot R_{\text{dl}}}{R_{\text{po}} + R_{\text{dl}}} \right)^{\frac{1-\alpha_{\text{dl}}}{\alpha_{\text{dl}}}} \quad (\text{Eq 8})$$

In the above equations, R_{sol} is the solution or medium resistance, Q_{coat} is the CPE of a coating, R_{po} is the resistance of the electrolyte in the coating pores, Q_{dl} is the CPE of the electrical double layer, and R_{dl} is the charge transfer resistance. Table 2 summarizes the fitted element values extracted from the EIS spectra by using the equivalent circuit shown in Fig. 11.

The equivalent circuit model $R_{\text{sol}}(Q_{\text{coat}}(R_{\text{po}}(Q_{\text{dl}}(R_{\text{dl}}W))))$ (Fig. 11a) represents the electrochemical corrosion process of coating 1. Since a diffusion process never comes for coating 2, $R_{\text{sol}}(Q_{\text{coat}}(R_{\text{po}}(Q_{\text{dl}}R_{\text{dl}})))$ is proposed in Fig. 11(b).

To understand the corrosion mechanisms of coatings 1 and 2, and better handle the data in Table 2, further interpretation has been schematically depicted in Fig. 12(a) and (b). There is no doubt that the denser a coating, the better anticorrosion property of the coating is, which can separate substrate from a corrosive medium completely. As shown in Fig. 12(a), the coating 1 has abundant voids and defects, which are preferential diffusion paths for corrosive species of H_2O , Na^+ , H^+ , OH^- , $\text{B}_4\text{O}_7^{2-}$, etc., in borax aqueous solution. By contrast, choosing phenolic modified aromatic amine as the curing agent, coating 2 has less voids and defects than coating 1 (Fig. 12b). Therefore, it is inevitable that there must be some pinholes microstructurally existing in the coating, which connect with each other to form sub-channels after a long time of immersion, allowing only small molecules of corrosive medium to penetrate through and corrode the inner substrate (Ref 38). Evidently, coating 2 behaves better on anticorrosion property.

The change of equivalent circuit parameters with the immersion time is used to reflect the change of electrochemical properties of the coated system (Ref 39). $C_{\text{eff,coat}}$ is related to

the intrinsic dielectric properties of the coating (Ref 22), which reflects the water uptake of the coating (Ref 1). $C_{eff,coat}$ ($k\epsilon A/d$) increases with increasing water uptake (Ref 40, 41), where k is the dielectric constant of free space, ϵ is the dielectric constant of the polymer, A is the exposed surface area, and d is the thickness of the coating. $C_{eff,coat}$ is quite sensitive to water uptake since the dielectric constant of water is about 20 times larger than that of the coating (Ref 28). The histograms in Fig. 13(a) show the variation trend of $C_{eff,coat}$ for coatings 1 and 2 with immersion time. The variation of $C_{eff,coat}$ for coating 1 presents a clear tendency to increase along the immersion time, while that for coating 2 is basically seen to be invariable. Meanwhile, the values of $C_{eff,coat}$ for coating 2 are significantly lower than that for coating 1. Lower $C_{eff,coat}$ indicates better water resistance for coating 2, which signifies that the barrier property of the coating can be improved effectively by selecting HN01 as curing agent.

It has been pointed out that R_{po} is inversely proportional to the defects (pores) in a film, which reflects porosity of coatings and the anti-penetrating ability of the coating to the electrolyte solution (Ref 22, 29, 42). As shown in Fig. 13(b), the values of R_{po} for both coatings 1 and 2 increase and then decrease, but with different peak occurring at different time. This may result from the passivation and accumulation of insoluble corrosion products of coating which could seal the pore channels of the polymer, further inhibiting the diffusion of the corrosive species at the early stage of immersion (Ref 43). Besides, the R_{po} value of coating 2 is comparatively larger, especially after immersion for 576 h. It is by more than 3 orders of magnitude larger than that of coating 1, which demonstrates that the porosity of coating 2 is relatively lower and degradation phenomenon is more difficult to happen.

Double-layer capacitance C_{dl} and polarization resistance R_{dl} are two parameters used to specify the delamination of the top coat and the onset of corrosion at the interface (Ref 44), of which $C_{eff,dl}$ obtained is proportional to the exposed metal surface area in contact with the electrolyte (Ref 45). Also, R_{dl} is a measure of the resistance to the electron transfer across the metal surface and is inversely proportional to corrosion rate (Ref 46). The corrosion has taken place at the bottom of the pores as evidenced from the increase in $C_{eff,dl}$ value for both coatings 1 and 2 with a decrease in R_{dl} value (Fig. 13c and d). The developments of pathways inside the coating account for a prominent increase in the $C_{eff,dl}$ value. Though coating 2 presents higher $C_{eff,dl}$ value in the earlier stage of immersion, the magnitude of its increase is much lower than that of coating 1. In the later stage, low $C_{eff,dl}$ value observed on coating 2 demonstrates low extent of detachment between the coating and substrate. It can be detected that R_{dl} possesses the similar varying tendency with R_{po} for both coatings 1 and 2. And coating 2 presents higher R_{dl} value compared with coating 1, which means lower corrosion rate for coating 2. In addition, it is worth noting that Warburg resistance keeps increasing for coating 1 (Fig. 13e), which indicates that the ability of diffusion controlled in electrochemical reactions becomes stronger for coating 1, as stated before.

In general, a coated metal system which performs well in corrosion is characterized by high resistances R_{po} and R_{dl} , and lower capacitances $C_{eff,coat}$ and $C_{eff,dl}$, as well as high Warburg impedance W , as compared with poor systems (Ref 47). Consequently, coating 2 performs best in the resistance to corrosion, and it inhibits effectively transport of electrolyte in the coating.

4. Conclusions

The development of two new anticorrosive coatings used in 60 °C borax aqueous solution has been studied in the work. As compared with coating cured by aromatic ring aliphatic amine, the water absorption and contact angle of the phenolic-epoxy/tetraglycidyl metaxyle diamine composite coating were reduced significantly by selecting phenolic modified aromatic amine. Illustrated by 3D confocal images, the surface roughness of the coating cured by phenolic modified aromatic amine was smaller; hence, the surface area for the corrosion attack becomes smaller. Observed from the cross section of coatings, the obvious corrosive products appeared for coating cured with modified aromatic ring aliphatic amine, while it remained intact for coating cured with phenolic modified aromatic amine, which showed remarkable corrosion resistance and difficult accessibility of water to the coating/substrate interface. No obvious decay in the Raman signal was observed, which indicated that the cross-linked structure of coating cured by phenolic modified aromatic amine was very stable during the corrosive immersion. As compared with coating cured by aromatic ring aliphatic amine, the coating cured by phenolic modified aromatic amine performed well in corrosion resistance and was characterized by high resistances (R_{po} and R_{dl}), lower capacitances ($C_{eff,coat}$ and $C_{eff,dl}$) as well as no Warburg impedance (W), which effectively inhibit the transport of water in the coating.

Acknowledgments

This work was supported by the Key Technology of Corrosion Control on Wind Power Equipment Academician Workstation Project (Grant Numbers 2013B090400023) and Henan science and technology achievement transformation project of Chinese Academy of Sciences. The authors are grateful to Ms. X. Xin for her support to the Raman spectrum analysis.

References

1. C.L. Zhou, X. Lu, Z. Xin, and J. Liu, Corrosion Resistance of Novel Silane-Functional Polybenzoxazine Coating on Steel, *Corros. Sci.*, 2013, **70**, p 145–151
2. M.L. Jiao, K. Yang, J. Cao, Q. Diao, W.X. Zhang, and M.H. Yu, Influence of Epichlorohydrin Content on Structure and Properties of High-ortho Phenolic Epoxy Fibers, *J. Appl. Polym. Sci.*, 2016, **133**, p 43375–43381
3. C.M. Satheesh, M.R. Temina, and K. Sunitha, Allyl Ether of Aralkyl Phenolic Resin with Low Melt Viscosity and Its Alder-ene Blends with Bismaleimide: Synthesis, Curing, and Laminate Properties, *Polym. Adv. Technol.*, 2014, **25**, p 881–890
4. S. Rimdusit, P. Jongvisuttisun, C. Jubsilp, and W. Tanthapanichakoon, Highly Processable Ternary Systems Based on Benzoxazine, Epoxy, and Phenolic Resins for Carbon Fiber Composite Processing, *J. Appl. Polym. Sci.*, 2009, **111**, p 1225–1234
5. J. Cech and B. Kretow, The Effectiveness of Toughening Technologies on Multifunctional Epoxy Resin Systems, *Surf. Coat. Aust.*, 2003, **40**, p 19–23
6. P.J. Xu and F.P. Yang, Modification of Phenolic Resin Composites by Hyperbranched Polyborate and Polybenzoxazine, *Polym. Compos.*, 2012, **33**, p 1960–1968
7. M.W. Wang, H.Y. Wu, and M.S. Lin, Synthesis, Curing Behavior and Properties of Siloxane and Imide-Containing Tetrafunctional Epoxy, *J. Polym. Res.*, 2008, **15**, p 1–9
8. I. Santana, A. Pepe, W. Schreiner, S. Pellice, and S. Cere, Hybrid Sol-Gel Coatings Containing Clay Nanoparticles for Corrosion Protection of Mild Steel, *Electrochim. Acta*, 2016, **203**, p 396–403

9. M.D. Destreri, J. Vogelsang, L. Fedrizzi, and F. Deflorian, Water Up-Take Evaluation of New Waterborne and High Solid Epoxy Coatings. Part II: Electrochemical Impedance Spectroscopy, *Prog. Org. Coat.*, 1999, **37**, p 69–81
10. G.K. van der Wel and O.C.G. Adan, Moisture in Organic Coatings—A Review, *Prog. Org. Coat.*, 1999, **37**, p 1–14
11. J. Hu, J. Zhang, D. Xie, and C.N. Cao, Water Transport in Organic Coatings (II) a Complicated Actual Trend, *J. Chin. Soc. Corros. Prot.*, 2002, **22**, p 371–374
12. Y. Liu, J.G. Wang, L. Liu, Y. Li, and F.H. Wang, Study of the Failure Mechanism of an Epoxy Coating System Under High Hydrostatic Pressure, *Corros. Sci.*, 2013, **74**, p 59–70
13. D.Y. Gao, R.B. Heimann, J. Lerchner, J. Seidel, and G. Wolf, Development of a Novel Moisture Sensor Based on Superabsorbent Poly(acrylamide)-montmorillonite Composite Hydrogels, *J. Mater. Sci.*, 2001, **36**, p 4567–4571
14. A. Abdal-Hay, M. Dewidar, and J.K. Lim, Biocorrosion Behavior and Cell Viability of Adhesive Polymer Coated Magnesium Based Alloys for Medical Implants, *Appl. Surf. Sci.*, 2012, **261**, p 536–546
15. E. Budke, J. Krempel-Hesse, H. Maidhof, and H. Schussler, Decorative Hard Coatings with Improved Corrosion Resistance, *Surf. Coat. Technol.*, 1999, **112**, p 108–113
16. W. Funke, Problems and Progress in Organic Coatings Science and Technology, *Prog. Org. Coat.*, 1997, **31**, p 5–9
17. M.B. Valcarce and M. Vazquez, Carbon Steel Passivity Examined in Alkaline Solutions: The Effect of Chloride and Nitrite Ions, *Electrochim. Acta*, 2008, **53**, p 5007–5015
18. M. Skrifvars, P. Niemela, R. Koskinen, and O. Hormi, Process Cure Monitoring of Unsaturated Polyester Resins, Vinyl Ester Resins, and Gel Coats by Raman Spectroscopy, *J. Appl. Polym. Sci.*, 2004, **93**, p 1285–1292
19. M.A. Gauthier, I. Stangel, T.H. Ellis, and X.X. Zhu, A New Method for Quantifying the Intensity of the C=C Band of Dimethacrylate Dental Monomers in Their FTIR and Raman Spectra, *Biomaterials*, 2005, **26**, p 6440–6448
20. E. Jerusha, S.S. Kirupavathy, and R. Gopalakrishnan, Spectral, Optical and Dielectric Analyses on L-lysine P-nitrophenolate Rnonohydrate Organic Crystals, *Optik*, 2016, **127**, p 420–427
21. F.T. Cao, J. Wei, J.H. Dong, and W. Ke, The Corrosion Inhibition Effect of Phytic Acid on 20SiMn Steel in Simulated Carbonated Concrete Pore Solution, *Corros. Sci.*, 2015, **100**, p 365–376
22. M.C. Yan, C.A. Vetter, and V.J. Gelling, Corrosion Inhibition Performance of Polypyrrole Al Flake Composite Coatings for Al Alloys, *Corros. Sci.*, 2013, **70**, p 37–45
23. H.W. Shi, F.C. Liu, L.H. Yang, and E.H. Han, Characterization of Protective Performance of Epoxy Reinforced with Nanometer-Sized TiO₂ and SiO₂, *Prog. Org. Coat.*, 2008, **62**, p 359–368
24. R. Hirayama and S. Haruyama, Electrochemical Impedance for Degraded Coated Steel Having Pores, *Corrosion*, 1991, **47**, p 952–958
25. I. Milosev, Z. Jovanovic, J.B. Bajat, R. Jancic-Heinemann, and V.B. Miskovic-Stankovic, Surface Analysis and Electrochemical Behavior of Aluminum Pretreated by Vinyltriethoxysilane Films in Mild NaCl Solution, *J. Electrochem. Soc.*, 2012, **159**, p C303–C311
26. M.F. Montemor, A.M. Cabral, M.L. Zheludkevich, and M.G.S. Ferreira, The Corrosion Resistance of Hot Dip Galvanized Steel Pretreated with Bis-functional Silanes Modified with Microsilica, *Surf. Coat. Technol.*, 2006, **200**, p 2875–2885
27. C. Liu, Q. Bi, A. Leyland, and A. Matthews, An Electrochemical Impedance Spectroscopy Study of the Corrosion Behaviour of PVD Coated Steels in 0.5 N NaCl Aqueous Solution: Part II. EIS Interpretation of Corrosion Behaviour, *Corros. Sci.*, 2003, **45**, p 1257–1273
28. F. Mansfeld, Use of Electrochemical Impedance Spectroscopy for the Study of Corrosion Protection by Polymer Coatings, *J. Appl. Electrochem.*, 1995, **25**, p 187–202
29. X.W. Liu, J.P. Xiong, Y.W. Lv, and Y. Zuo, Study on Corrosion Electrochemical Behavior of Several Different Coating Systems by EIS, *Prog. Org. Coat.*, 2009, **64**, p 497–503
30. M.C. Yan, J. Xu, L.B. Yu, T.Q. Wu, C. Sun, and W. Ke, EIS Analysis on Stress Corrosion Initiation of Pipeline Steel Under Disbonded Coating in Near-Neutral pH Simulated Soil Electrolyte, *Corros. Sci.*, 2016, **110**, p 23–34
31. L. Kouisni, M. Azzi, F. Dalard, and S. Maximovitch, Phosphate Coatings on Magnesium Alloy AM60 Part 2: Electrochemical Behaviour in Borate Buffer Solution, *Surf. Coat. Technol.*, 2005, **192**, p 239–246
32. J. Bisquert, G. Garcia-Belmonte, P. Bueno, E. Longo, and L.O.S. Bulhoes, Impedance of Constant Phase Element (CPE)-Blocked Diffusion in Film Electrodes, *J. Electroanal. Chem.*, 1998, **452**, p 229–234
33. B. Rosborg, T. Kosec, A. Kranjc, J.S. Pan, and A. Legat, Electrochemical Impedance Spectroscopy of Pure Copper Exposed in Bentonite under Oxidic Conditions, *Electrochim. Acta*, 2011, **56**, p 7862–7870
34. R.N. Deo, N. Biribilis, and J.P. Cull, Measurement of Corrosion in Soil Using the Galvanostatic Pulse Technique, *Corros. Sci.*, 2014, **80**, p 339–349
35. M. Mouanga, M. Puiggali, and O. Devos, EIS and LEIS Investigation of Aging Low Carbon Steel with Zn-Ni Coating, *Electrochim. Acta*, 2013, **106**, p 82–90
36. A. Singh, I. Ahamad, V.K. Singh, and M.A. Quraishi, Inhibition Effect of Environmentally Benign Karanj (*Pongamia pinnata*) Seed Extract on Corrosion of Mild Steel in Hydrochloric Acid Solution, *J. Solid State Electrochem.*, 2011, **15**, p 1087–1097
37. B. Hirschorn, M.E. Orazem, B. Tribollet, V. Vivier, I. Frateur, and M. Musiani, Determination of Effective Capacitance and Film Thickness from Constant-Phase-Element Parameters, *Electrochim. Acta*, 2010, **55**, p 6218–6227
38. D.Y. Yu, J.T. Tian, J.H. Dai, and X. Wang, Corrosion Resistance of Three-Layer Superhydrophobic Composite Coating on Carbon Steel in Seawater, *Electrochim. Acta*, 2013, **97**, p 409–419
39. X.M. Su, Q. Zhou, Q.Y. Zhang, Y. Zhang, and H. Zhang, Study on the Deterioration Process of Bipolar Coating Using Electrochemical Impedance Spectroscopy, *Appl. Surf. Sci.*, 2011, **257**, p 6095–6101
40. F. Mansfeld and C.H. Tsai, Determination of Coating Deterioration With EIS. 1. Basic Relationships, *Corrosion*, 1991, **47**, p 958–963
41. F. Mansfeld, Evaluation of Corrosive Degradation in Coated Steel Using Alternating Current Impedance Spectroscopy—Discussion, *Corrosion*, 1996, **52**, p 417–418
42. H. Yun, J. Li, H.B. Chen, and C.J. Lin, A Study on the N-, S- and Cl-Modified Nano-TiO₂ Coatings for Corrosion Protection of Stainless Steel, *Electrochim. Acta*, 2007, **52**, p 6679–6685
43. J.G. Liu, G.P. Gong, and C.W. Yan, EIS Study of Corrosion Behaviour of Organic Coating/Dacromet Composite Systems, *Electrochim. Acta*, 2005, **50**, p 3320–3332
44. F. Mansfeld, Models for the Impedance Behavior of Protective Coatings and Cases of Localized Corrosion, *Electrochim. Acta*, 1993, **38**, p 1891–1897
45. W. Li, H. Tian, and B. Hou, Corrosion Performance of Epoxy Coatings Modified by Nanoparticulate SiO₂, *Mater. Corros.*, 2012, **63**, p 44–53
46. H.H. Hassan, E. Abdelghani, and M.A. Amin, Inhibition of Mild Steel Corrosion in Hydrochloric Acid Solution by Triazole Derivatives—Part I. Polarization and EIS Studies, *Electrochim. Acta*, 2007, **52**, p 6359–6366
47. N. Tang, W.J. vanOoij, and G. Gorecki, Comparative EIS Study of Pretreatment Performance in Coated Metals, *Prog. Org. Coat.*, 1997, **30**, p 255–263